



# Scaling analysis for rapid estimation of lack of fusion porosity in laser powder bed fusion

Pramod R. Zagade<sup>a,b</sup>, B. P. Gautham<sup>a</sup>, Amitava De<sup>b</sup> and Tarasankar DebRoy<sup>c</sup>

<sup>a</sup>TCS Research, Tata Consultancy Services, Pune, India; <sup>b</sup>Department of Mechanical Engineering, Indian Institute of Technology Bombay, Mumbai, India; <sup>c</sup>Department of Materials Science and Engineering, The Pennsylvania State University, State College, PA, USA

## ABSTRACT

Lack-of-fusion porosity due to insufficient melting of the adjacent tracks and successive layers is a persistent problem in laser powder bed fusion (LPBF). A novel functional relation is proposed here following dimensional analysis for rapid estimation of the lack-of-fusion porosity fraction as a function of important process variables and alloy properties. The estimated values of the porosity fractions are found to be in fair agreement with the corresponding independent experimentally measured results for LPBF of five commonly used alloys for a wide range of process conditions. The proposed functional relation is used further to construct a set of process maps that can aid in the selection of important LPBF conditions to avoid lack-of-fusion porosity on the shop floor without doing any calculations.

## ARTICLE HISTORY

Received 21 August 2022  
Revised 17 December 2022  
Accepted 30 December 2022

## KEYWORDS

Laser powder bed fusion (LPBF); dimensional analysis; lack-of-fusion porosity; porosity fraction

## 1. Introduction

Lack-of-fusion porosities between the tracks and layers affect the part density and act as crack initiation sites resulting in reduced durability of parts made by laser powder bed fusion (LPBF) [1–3]. These porosities arise due to small melt pools, which fail to adequately overlap the adjacent tracks and deposited layers and result in un-melted regions remaining as pores in the final part [1,2]. Experimental investigations showed that higher power density and smaller hatch spacing could reduce lack-of-fusion porosity for LPBF of titanium [4], aluminum [5], and nickel [6] alloys. These studies required a high volume of experiments over a large process parameter space. Attempts are ongoing to develop empirical relations and scaling laws to evaluate the propensity of an LPBF condition to lack-of-fusion porosity in terms of melt pool dimensions and powder properties [6–9]. Numerical models have been used to compute the melt pool dimensions and determine porosity fractions for LPBF of nickel [10], stainless steel [11], titanium [12,13], and aluminum [14] alloys. The computationally intensive nature of these models to simulate the LPBF process has remained a critical challenge [10,15,16]. In contrast, analytical heat conduction models [17,18] can rapidly calculate the melt pool dimensions and support scaling relations for quick evaluation of lack-of-fusion porosity for high throughput screening during the initial design stages of LPBF.


Here, we propose a novel scaling analysis to identify a set of non-dimensional terms to identify

the susceptibility of an LPBF condition to lack-of-fusion porosity. These non-dimensional terms involve important LPBF variables, alloy properties, and melt pool dimensions, which are computed from a well-established analytical heat conduction model [19]. The sensitivity of the lack-of-fusion porosity to the non-dimensional terms is tested using measured porosity fraction data from the literature for LPBF of five commonly used powders. A unique relation for porosity fraction as a function of the non-dimensional terms is established and tested extensively. Finally, a set of porosity fraction maps is developed using the functional relation for the selection of appropriate LPBF variables to reduce lack-of-fusion porosity.

## 2. Dimensional analysis

The dimensional analysis is carried out to identify a set of non-dimensional terms, which can uncover the role of important LPBF variables on the evolution of lack-of-fusion porosity. Table 1 shows the variables for the dimensional analysis. The susceptibility to porosity is denoted by the dimensionless porosity fraction ( $\phi$ ) and its values are estimated from the measured extent of pores [4] or relative density [20] of a part. Among several LPBF variables, the laser power ( $P$ ), scanning speed ( $v$ ), layer thickness ( $\lambda$ ), and hatch spacing ( $\delta$ ) are considered to be important. An increase in the laser power results in a greater rate of melting of the powder particles and reduces the chance of lack-of-fusion porosity

**CONTACT** Amitava De  [amit@iitb.ac.in](mailto:amit@iitb.ac.in); [de.amitava1967@gmail.com](mailto:de.amitava1967@gmail.com)

 Supplemental data for this article can be accessed here. <https://doi.org/10.1080/13621718.2022.2164830>

**Table 1.** Variables used for dimensional analysis.

Variable	Symbol	Unit	Dimension
Laser power	$P$	W	$ML^2T^{-3}$
Scanning speed	$v$	m/s	$LT^{-1}$
Layer thickness	$\lambda$	m	L
Hatch spacing	$\delta$	m	L
Melt pool width	$w$	m	L
Melt pool depth	$d$	m	L
Enthalpy at melting	$H_m$	$J/m^3$	$ML^{-1}T^{-2}$
Porosity fraction	$\phi$	—	$M^0L^0T^0$

[20]. In contrast, an increase in the scanning speed reduces the rate of heat input per unit length of a track leading to inadequate melting of powder and porosities in the final part [21,22]. An increase in both the layer thickness and hatch spacing requires the melting of a greater volume of powder to avoid porosity between tracks and layers [4,5,23]. Among the powder properties, the enthalpy of melting per unit volume ( $H_m$ ) provides a measure of the amount of energy required for an alloy for complete melting and is therefore considered an important variable. Lastly, the melt pool width ( $w$ ) and depth ( $d$ ) are also deemed to be essential variables for identifying lack-of-fusion porosity as inadequate pool dimensions lead to unfused regions and voids between tracks and layers.

Considering the eight variables and three fundamental dimensions (Table 1), five dimensionless terms are formed and two of them are combined further to obtain four unique dimensionless terms as

$$\pi_1 = \phi \quad (1)$$

$$\pi_2 = \frac{\delta}{w} \quad (2)$$

$$\pi_3 = \frac{\lambda}{d} \quad (3)$$

$$\pi_4 = \frac{P}{(v\delta\lambda)H_m} \quad (4)$$

The detailed steps to form these dimensionless terms are presented in Appendix. The term  $\pi_1$  represents the extent of lack-of-fusion porosity in LPBF in terms of porosity fraction. The term  $\pi_2$  depicts a ratio of the hatch spacing ( $\delta$ ) and the melt pool width ( $w$ ). Likewise, the term  $\pi_3$  represents a ratio of the layer thickness ( $\lambda$ ) and the melt pool depth ( $d$ ). In turn, both  $\pi_2$  and  $\pi_3$  directly influence the lack-of-fusion porosity in LPBF. The term  $\pi_4$  represents a dimensionless ratio of the input energy per unit volume and the energy required for melting the alloy. As a result, the term  $\pi_4$  accounts for the influence of LPBF variables and material properties across different alloys and inversely affects the lack-of-fusion porosity.

In the following section, the sensitivity of the terms  $\pi_2$ ,  $\pi_3$ , and  $\pi_4$  to important process variables and their influences on the  $\pi_1$  term are examined for LPBF of five commonly used alloys. The term  $\pi_1$  is considered equal to the measured porosity fraction and the terms  $\pi_2$ ,  $\pi_3$ , and  $\pi_4$  are calculated considering the corresponding LPBF conditions from the literature. An analytical heat conduction model [19] is used to compute the melt pool dimensions  $w$  and  $d$ , which are required to calculate  $\pi_2$  and  $\pi_3$ , respectively. Table 2 provides the range of LPBF conditions and material properties of the alloys, which are used here. The analytically computed melt pool dimensions  $w$  and  $d$  are presented in the form of process maps as function of laser beam power and scanning speed as Figure S1 in a ‘Supplemental Document’.

### 3. Analysis of dimensionless variables

Figure 1 shows the influence of the dimensionless term  $\pi_2$ , i.e. the ratio of hatch spacing ( $\delta$ ) and analytically computed melt pool width ( $w$ ) on the experimentally measured porosity fractions (i.e.  $\pi_1$ ) for LPBF of five alloys. The values of the porosity fraction are almost

**Table 2.** Ranges of process conditions and measured porosity fraction values for LPBF of Ti6Al4V [4,20,24], SS316L [22,23,25,26], AlSi10Mg [5,27], H13 [28,29], and IN718 [6,21,30] powder and material properties [31–33] used for the analytical model [19].

Parameter	Ti6Al4V	SS316L	AlSi10Mg	IN718	H13
Laser power, $P$ (W)	40–200	90–300	150–350	90–370	150–300
Scanning speed, $v$ (m/s)	0.12–1.56	0.3–2.8	0.5–2.5	0.4–1.6	0.4–1.0
Layer thickness, $\lambda$ ( $\mu\text{m}$ )	30–50	25–40	30–90	25–60	40
Hatch spacing, $\delta$ ( $\mu\text{m}$ )	100	80–120	45–130	80–120	80–120
Porosity fraction, $\phi$	0.001–0.220	0.001–0.160	0.002–0.160	0.002–0.130	0.001–0.070
Density, $\rho$ ( $\text{kg}/\text{m}^3$ )	4200	7400	2610	7700	7100
Solidus, liquidus temperatures, ( $T_s, T_L$ ) (K)	1878, 1923	1658, 1723	823, 850	1533, 1609	1585, 1723
Enthalpy of melting per unit volume, $H_m$ ( $\text{J}/\text{m}^3$ )	$6.86 \times 10^9$	$9.47 \times 10^9$	$2.84 \times 10^9$	$8.47 \times 10^9$	$7.94 \times 10^9$
Conductivity, $k$ (W/mK)	$8.7 \times [1 + (1.18 \times 10^{-3} \times T)]$	$11.3 \times [1 + (0.89 \times 10^{-3} \times T)]$	$118 \times [1 + (0.01 \times 10^{-3} \times T)]$	$11.5 \times [1 + (1.06 \times 10^{-3} \times T)]$	$22.1 \times [1 + (0.76 \times 10^{-3} \times T)]$
Specific heat, $C$ (J/kgK)	$260 \times [1 + (1.18 \times 10^{-3} \times T)]$	$280 \times [1 + (0.89 \times 10^{-3} \times T)]$	$980 \times [1 + (0.01 \times 10^{-3} \times T)]$	$280 \times [1 + (1.06 \times 10^{-3} \times T)]$	$310 \times [1 + (0.76 \times 10^{-3} \times T)]$

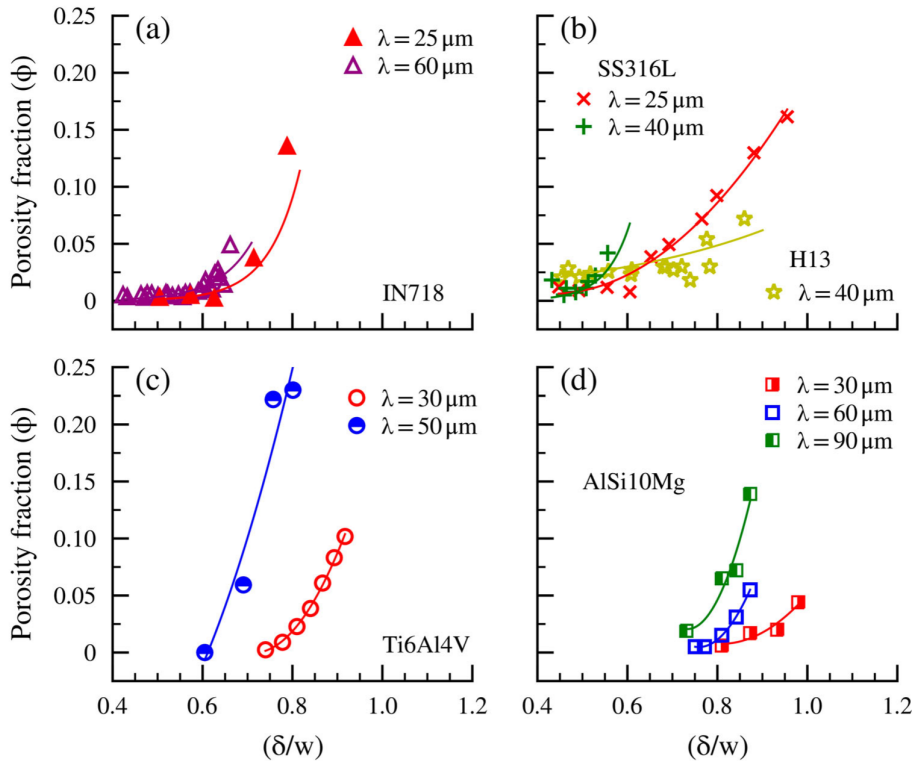


**Figure 1.** Experimentally measured porosity fraction ( $\phi$ ) as a function of the dimensionless term  $\pi_2$ , i.e.  $\delta/w$  for LPBF of five alloys for different values of layer thickness ( $\lambda$ ). The values of the measured porosity fractions are obtained from the literature as – Ti6Al4V [20,24], IN718 [6,21], SS316L [25,26], AlSi10Mg [27], and H13 [28,29].

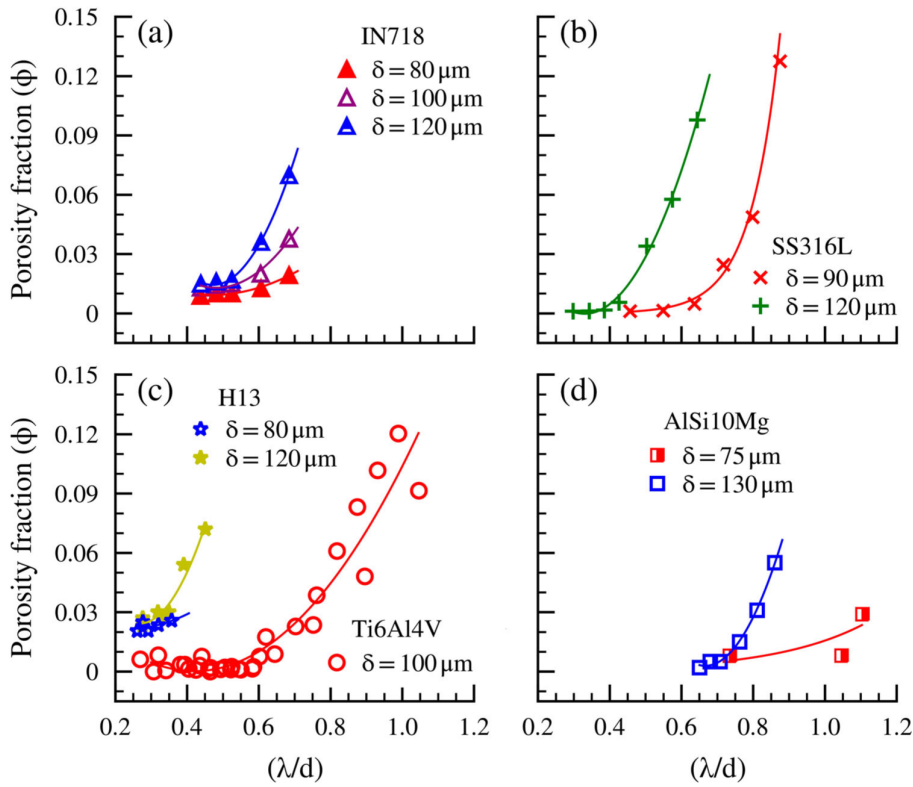
negligible at smaller values of  $\delta/w$  that confirm the formation of adequate melt pool sizes. The porosity fractions increase rapidly with an increase in the ratio of  $\delta/w$ , which indicates a smaller melt pool width in comparison to the hatch spacing. A comparison of Figure 1(a–d) shows that the porosity fractions for different alloys increase over varying ranges of  $\delta/w$ , which is attributed to diverse alloy properties and LPBF conditions. Further analysis shows that the nature of variation between the measured porosity fraction and the dimensionless term  $\delta/w$  is also dependent on the values of the layer thickness ( $\lambda$ ). This is intuitive as an increase in the layer thickness requires the melting of a greater volume of powder mass to avoid unmelted voids between the layers. A comparison of Figure 1(c and d) shows a notable increase in the porosity fraction at higher values of the layer thickness ( $\lambda$ ) for LPBF of Ti6Al4V and AlSi10Mg.

Figure 1 shows that the dimensionless term  $\pi_2$ , i.e.  $\delta/w$  is an important variable to account for the lack-of-fusion porosity in LPBF but it is also required to account for the influence of the layer thickness ( $\lambda$ ), which is undertaken by the dimensionless term  $\pi_3$ , i.e. ( $\lambda/d$ ). Figure 2 shows the influence of the dimensionless term  $\lambda/d$  on the experimentally measured porosity fractions for the LPBF of five alloys. An increase in  $\lambda/d$  indicates a smaller melt pool depth in comparison to the layer thickness, which can result in an inadequate bonding between successive layers. The porosity fraction is

negligible at smaller values of  $\lambda/d$  and increases with an increase in  $\lambda/d$ . At a larger hatch spacing ( $\delta$ ), the porosity fractions readily increase with an increase in  $\lambda/d$ , which is intuitive since wider hatch spacing and greater layer thickness contribute to the propensity of increased unmelted regions between the adjacent tracks and layers, respectively (Figure 2(a–d)).

Figures 1 and 2 illustrate that the dimensionless terms  $\pi_2$  and  $\pi_3$  account for the influence of important LPBF variables on the porosity fractions but the nature of their influences is diverse for different alloys. A term that can take into account the variability arising out of alloy properties is therefore required, which is introduced by the dimensionless term  $\pi_4$ . Equation (4) shows that  $\pi_4$  is a ratio of the input energy per unit volume and the enthalpy of melting of an alloy. For a given LPBF condition, an alloy with higher enthalpy of melting will result in smaller melt pool sizes and be more susceptible to lack-of-fusion porosity. As a result, the experimentally measured porosity fractions for LPBF of all the five different alloys increase with  $1/\pi_4$  as shown in Figure 3. It is also noteworthy that for a given alloy, an increase in  $1/\pi_4$  indicates a relatively lower amount of input energy per unit volume of powder, which results in smaller melt pool sizes and increases susceptibility to lack-of-fusion porosity.

Overall, Figure 1–3 show that the three dimensionless terms  $\pi_2$ ,  $\pi_3$ , and  $\pi_4$  can collectively undertake the effect of the LPBF variables and alloy properties on the



**Figure 2.** Experimentally measured porosity fraction ( $\phi$ ) as a function of the dimensionless term  $\pi_2$ , i.e.  $\lambda/w$  for LPBF of five commonly used powder alloys for different values of hatch spacing ( $\delta$ ). The values of the experimentally measured porosity fractions are obtained from the literature as – Ti6Al4V [20], IN718 [30], SS316L [23,25], AlSi10Mg [5,27], and H13 [28,29].

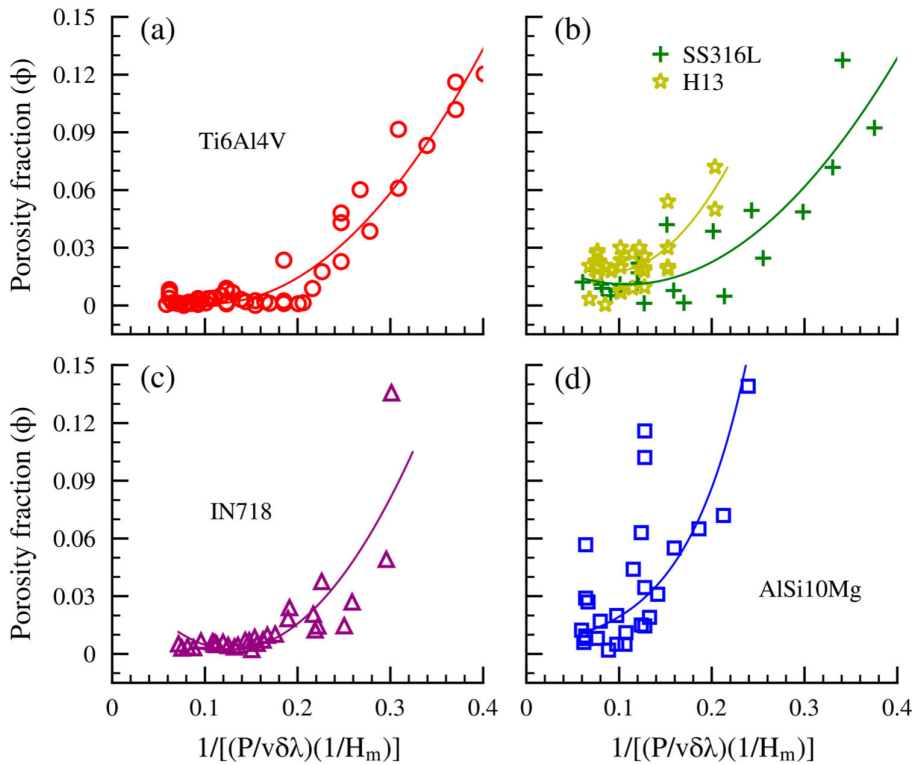


**Figure 3.** Experimentally measured porosity fraction as a function of  $1/(\pi_4)$  in LPBF processing of Ti6Al4V [4,20], IN718 [6,21], SS316L [22,25,26], AlSi10Mg [5,27], and H13 tool steel [28,29].

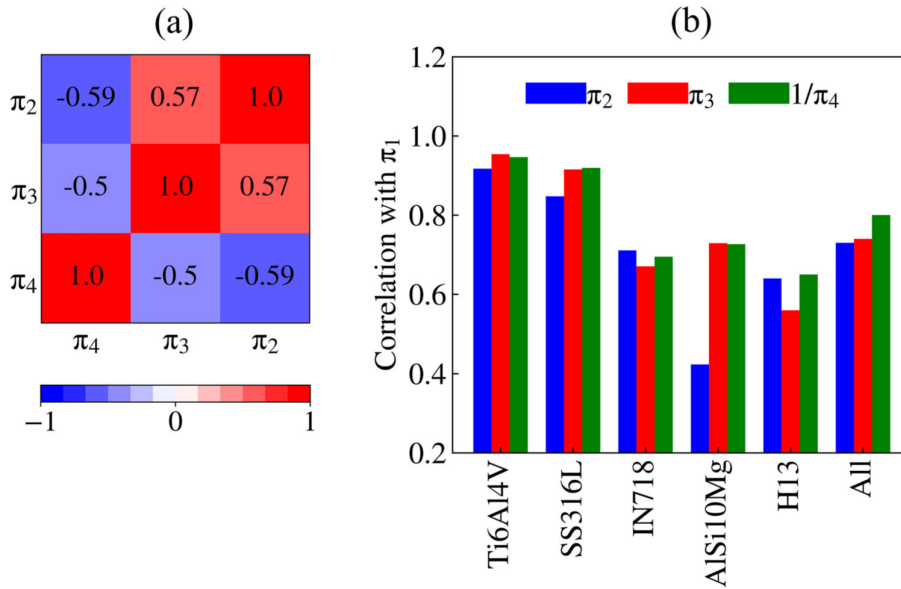


**Figure 4.** (a) Pearson correlation among the dimensionless terms  $\pi_2$ ,  $\pi_3$ , and  $\pi_4$  and (b) pair-wise correlation between porosity fraction  $\pi_1$  and each of the other three dimensionless terms  $\pi_2$ ,  $\pi_3$ , and  $\pi_4$ . The values of the correlation coefficients are computed considering 170 data sets of measured porosity fractions and the corresponding conditions for LPBF of Ti6Al4V [4,20], IN718 [6,21], SS316L [22,25,26], AlSi10Mg [5,27], and H13 tool steel [28,29].

propensity to porosity fractions in the final part. An effort is therefore presented next to develop a unique functional relation for an estimation of the porosity fraction as a function of  $\pi_2$ ,  $\pi_3$ , and  $\pi_4$ .

#### 4. Development of functional relationship

The correlations among the dimensionless terms  $\pi_2$ ,  $\pi_3$ , and  $\pi_4$  are examined first by calculating the Pearson correlation coefficients [34,35] for one hundred seventy sets of LPBF conditions, the corresponding calculated melt pool dimensions using an analytical model [19], and the respective measured values of the porosity fractions from literature. Figure 4(a) shows a moderately positive correlation between the terms  $\pi_2$  and  $\pi_3$ , which is attributed to the similar nature of variations in these two terms for the range of LPBF conditions. In other words, a variation in the LPBF conditions such as laser power and scanning speed affects both melt pool dimensions fairly similarly, which are the key variables in  $\pi_2$  and  $\pi_3$ . In contrast, a decrease in the dimensionless term  $\pi_4$  indicates either an alloy with a higher enthalpy at melting or a lower amount of energy per unit volume of powder, and both result in smaller melt pool dimensions. As a result, both  $\pi_2$  and  $\pi_3$  show a moderately negative correlation with the dimensionless term  $\pi_4$  as shown in Figure 4(a). A correlation coefficient value of greater than 0.9 is commonly used in literature to recognize the redundancy of variables due to a strong interrelation [36–38]. The absolute magnitudes of all the correlation coefficients in Figure 4(a) are smaller than 0.6. All three  $\pi$  terms, i.e.  $\pi_2$ ,  $\pi_3$ , and  $\pi_4$  are therefore considered constituents for the functional relationship to estimate the lack-of-fusion porosity fraction in LPBF.

Figure 4(b) shows the associative nature between the porosity fraction  $\pi_1$  and each of the three dimensionless terms  $\pi_2$ ,  $\pi_3$ , and  $\pi_4$  in terms of the respective Pearson correlation coefficients. The correlation coefficients between the pair-wise  $\pi$  terms are calculated separately for each alloy and together for all five alloys. Figure 4(b) shows a fair correlation between the porosity fraction  $\pi_1$  and each of the dimensionless terms  $\pi_2$ ,  $\pi_3$ , and  $\pi_4$ . A slightly lesser value of the correlation coefficient between the porosity fraction  $\pi_1$  and the dimensionless term  $\pi_2$  for AlSi10Mg alloy is attributed to the variability in the data sets for a wide range of

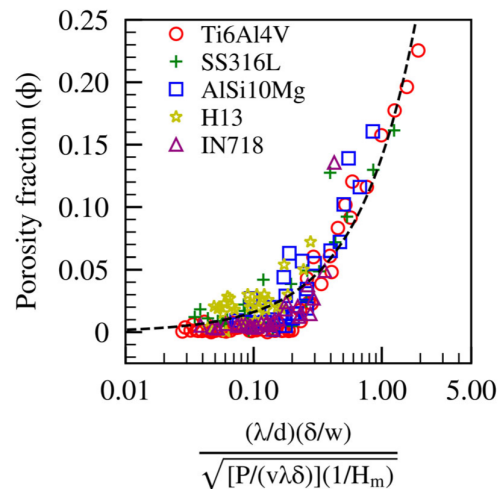


**Figure 5.** Experimentally measured porosity fraction ( $\phi$ ) and the corresponding calculated values using Equation (6) (represented by the black dashed best-fit line) for LPBF of Ti6Al4V [4,20], SS316L [22,25,26], AlSi10Mg [5,27], IN718 [6,21], and H13 tool steel [28,29].

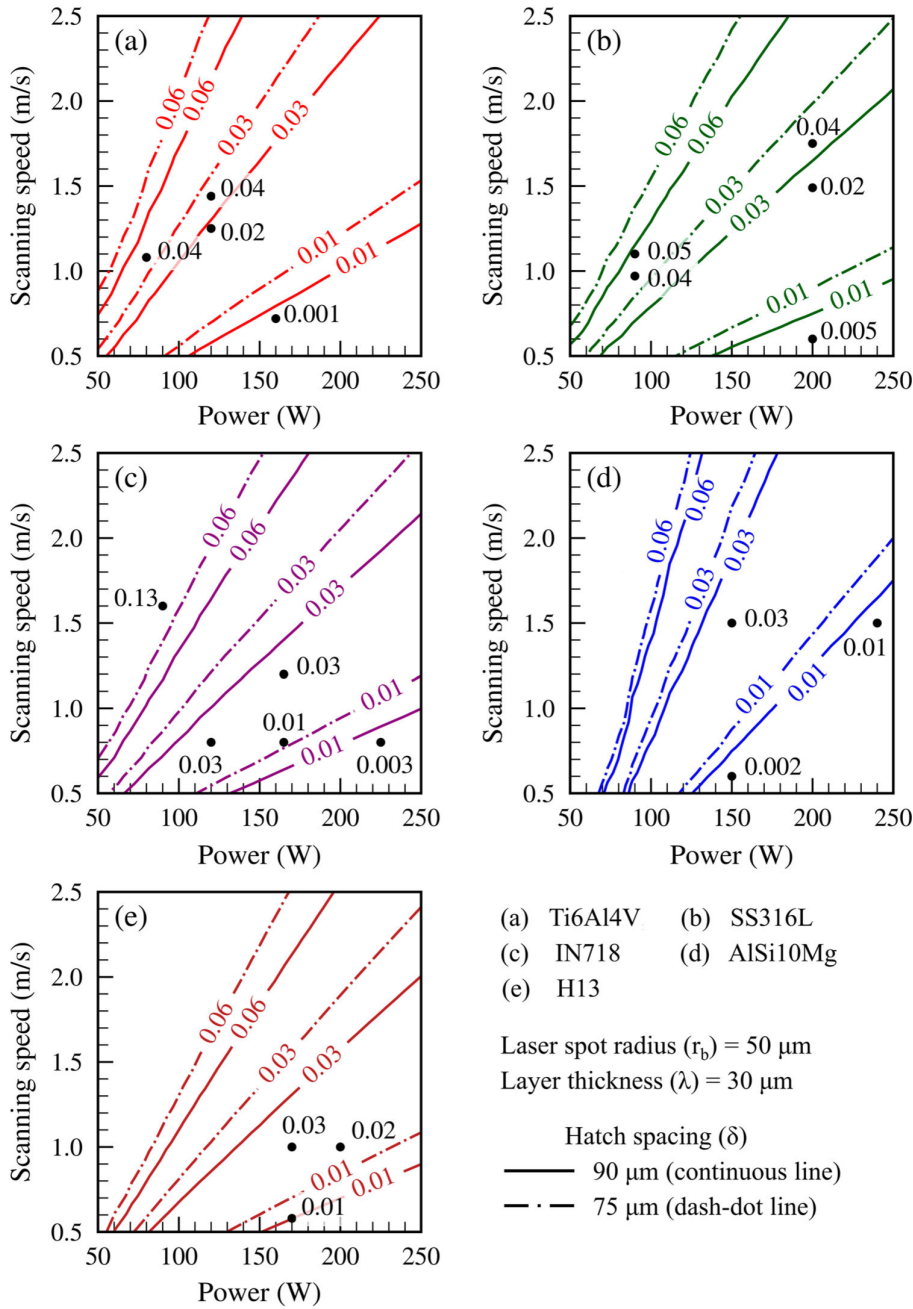


**Figure 6.** Process maps showing iso-contours of computed porosity fraction ( $\phi$ ) for LPBF of five alloys as a function of laser power and scanning speed. A few experimentally measured porosity fractions [5,20–22,25,26,41,42] for similar process conditions are shown as black dots.

hatch spacing and layer thicknesses. The values of the individual correlation coefficients between  $\pi_1$  and each of  $\pi_2$ ,  $\pi_3$ , and  $\pi_4$  terms are found to be in the range of 0.75–0.80 when the measured porosity fraction values are considered for all the alloys. These values indicate that a consistent relationship for  $\pi_1$  can be formed as a function of  $\pi_2$ ,  $\pi_3$ , and  $\pi_4$ . A functional relationship is therefore considered among the  $\pi$  terms as

$$\pi_1 = f(\pi_2, \pi_3, 1/\pi_4) \quad (5)$$

A set of 170 experimentally measured porosity fraction values from the literature for LPBF of five alloys

and the corresponding process conditions are used next to find the best fit functional relation for  $\pi_1$  as a function of  $\pi_2$ ,  $\pi_3$ , and  $\pi_4$ , which is expressed in an explicit form as

$$\phi = 0.14 \left[ \frac{(\lambda/d) (\delta/w)}{\sqrt{[P/(v\lambda\delta)] (1/H_m)}} \right]^{0.94} \quad (6)$$

Figure 5 shows the experimentally measured porosity fraction values from the literature for LPBF of five alloys and the best fit line with a correlation coefficient ( $R$ ) of 0.92. The parameter on the right-hand side in

Equation (6) includes three dimensionless terms and depicts a scaling factor to calculate the porosity fraction of a part as a function of important LPBF variables and alloy properties.

Figure 5 exhibits a fair estimation of the porosity fractions for a range of LPBF conditions across multiple alloys. A further improvement for accuracy in prediction warrants a detailed accounting of the underlying physical phenomena through comprehensive computational models. It is also noteworthy that the porosity can emerge from various sources such as lack of fusion, collapsing keyhole, entrapment of gases, and balling and spattering in the actual parts during LPBF [1,2]. The clear identification of the sources of porosity and quantification of their individual effect on the density of the final part is difficult and rarely reported in the literature. Nevertheless, it is worthwhile to probe into the potential range of the key LPBF process variables that can print metallic parts with a porosity fraction of 0.01 or lower to avoid lack-of-fusion porosity [39,40]. Equation (6) is therefore used further to construct porosity fraction maps, which can serve as a resource for the selection of important LPBF variables to minimize porosity.

## 5. Process maps

Figure 6(a–e) presents a set of porosity fraction maps as a function of laser power and scanning speed for two different hatch spacing for LPBF of five commonly used alloys. The porosity fraction increases with an increase in scanning speed and a decrease in the laser power, which is intuitive. For a given process condition and alloy, the tendency to form lack-of-fusion porosity reduces for a smaller hatch spacing. The lack-of-fusion porosity for LPBF of AlSi10Mg alloy is the most sensitive to the laser power whereas both laser power and scanning speed are important to mitigate lack-of-fusion porosity for the other four alloys. A few experimentally measured porosity fraction values from the literature [5,20–22,25,26,41,42] are shown in Figure 6(a–e), which are in fair proximity to the corresponding estimated contours.

In summary, a unique functional relation is developed using a scaling analysis with a set of dimensionless variables to estimate the lack-of-fusion porosity for LPBF of commonly used alloys. The proposed approach is useful for a fast and fairly reliable estimation of the lack-of-fusion porosity fractions in LPBF that involves numerous variables and their complex physical interactions. The proposed porosity fraction maps are useful for the rapid determination of the favorable parameter space to reduce the lack-of-fusion porosity.

## 6. Conclusions

A novel functional relation is developed using dimensional analysis for a fast and reliable estimation of the

lack-of-fusion porosity for LPBF of alloys. The lack-of-fusion porosity fractions are assessed as a function of important LPBF variables, alloy property, and analytically computed melt pool dimensions. The calculated results are tested rigorously with the corresponding measured porosity fractions for LPBF of five commonly used alloys. The proposed relationship is used to construct a set of porosity fraction maps that can help to select the permissible range of LPBF variables to minimize lack-of-fusion porosity. Following are the main conclusions.

- Three unique dimensionless variables, the ratio of hatch spacing to melt pool width, the layer thickness to melt pool depth, and the heat input per unit volume to the enthalpy of melting of an alloy are identified as valuable indicators to recognize the susceptibility of an LPBF condition to lack-of-fusion porosity.
- Two of the dimensionless variables, the ratio of hatch spacing to melt pool width, and the layer thickness to melt pool depth are found to directly influence the lack-of-fusion porosity. In contrast, the porosity fraction is inversely proportional to the ratio of the heat input per unit volume to the enthalpy of an alloy.
- A detailed analysis considering around one hundred seventy data sets for LPBF of five commonly used alloys from literature reveals strong correlations between each of the proposed dimensionless variables and the lack-of-fusion porosity fractions.
- A novel functional relationship is established to estimate the susceptibility of an LPBF condition to lack-of-fusion porosity in LPBF rapidly and fairly reliably as a collective function of the three dimensionless variables.
- The proposed functional relationship is used to develop porosity fraction maps as a function of laser power and scanning speed, which can help in high throughput screening of LPBF variables to avoid lack-of-fusion porosity in parts during practical design.

## Disclosure statement

No potential conflict of interest was reported by the author(s).

## ORCID

Amitava De  <http://orcid.org/0000-0002-3109-261X>

## References

- [1] Snow Z, Nassar AR, Reutzel EW. Invited review article: review of the formation and impact of flaws in powder bed fusion additive manufacturing. *Addit Manuf.* 2020;36:101457. DOI: 10.1016/j.addma.2020.101457
- [2] DebRoy T, Wei HL, Zuback JS, et al. Additive manufacturing of metallic components – process, structure

- and properties. *Prog Mater Sci.* 2018;92:112–224. DOI: [10.1016/j.pmatsci.2017.10.001](https://doi.org/10.1016/j.pmatsci.2017.10.001)
- [3] Macías JG S, Elangeswaran C, Zhao L, et al. Fatigue crack nucleation and growth in laser powder bed fusion AlSi10Mg under as built and post-treated conditions. *Mater Des.* 2021;210:110084. DOI: [10.1016/j.matdes.2021.110084](https://doi.org/10.1016/j.matdes.2021.110084)
  - [4] Kasperovich G, Haubrich J, Gussone J, et al. Correlation between porosity and processing parameters in TiAl6V4 produced by selective laser melting. *Mater Des.* 2016;105:160–170.
  - [5] Hastie JC, Kartal ME, Carter LN, et al. Classifying shape of internal pores within AlSi10Mg alloy manufactured by laser powder bed fusion using 3D X-ray micro computed tomography: influence of processing parameters and heat treatment. *Mater Charact.* 2020;163:110225. DOI: [10.1016/j.matchar.2020.110225](https://doi.org/10.1016/j.matchar.2020.110225)
  - [6] Wang Z, Liu M. Dimensionless analysis on selective laser melting to predict porosity and track morphology. *J Mater Process Technol.* 2019;273:116238. DOI: [10.1016/j.jmatprotec.2019.05.019](https://doi.org/10.1016/j.jmatprotec.2019.05.019)
  - [7] Gan Z, Kafka OL, Parab N, et al. Universal scaling laws of keyhole stability and porosity in 3D printing of metals. *Nat Commun.* 2021;12:2379. DOI: [10.1038/s41467-021-22704-0](https://doi.org/10.1038/s41467-021-22704-0)
  - [8] Rankouhi B, Agrawal AK, Pfefferkorn FE, et al. A dimensionless number for predicting universal processing parameter boundaries in metal powder bed additive manufacturing. *Manuf Lett.* 2021;27:13–17. DOI: [10.1016/j.mfgle.2020.12.002](https://doi.org/10.1016/j.mfgle.2020.12.002)
  - [9] Tang M, Pistorius PC, Beuth JL. Prediction of lack-of-fusion porosity for powder bed fusion. *Addit Manuf.* 2017;14:39–48. DOI: [10.1016/j.addma.2016.12.001](https://doi.org/10.1016/j.addma.2016.12.001)
  - [10] Bayat M, Mohanty S, Hattel JH. Multiphysics modelling of lack-of-fusion voids formation and evolution in IN718 made by multi-track/multi-layer L-PBF. *Int J Heat Mass Transf.* 2019;139:95–114. DOI: [10.1016/j.ijheatmasstransfer.2019.05.003](https://doi.org/10.1016/j.ijheatmasstransfer.2019.05.003)
  - [11] Bruna-Rosso C, Demir AG, Previtali B. Selective laser melting finite element modeling: validation with high-speed imaging and lack of fusion defects prediction. *Mater Des.* 2018;156:143–153. DOI: [10.1016/j.matdes.2018.06.037](https://doi.org/10.1016/j.matdes.2018.06.037)
  - [12] Panwisawas C, Qiu C, Anderson MJ, et al. Mesoscale modelling of selective laser melting: thermal fluid dynamics and microstructural evolution. *Comput Mater Sci.* 2017;126:479–490. DOI: [10.1016/j.commatsci.2016.10.011](https://doi.org/10.1016/j.commatsci.2016.10.011)
  - [13] Qiu C, Panwisawas C, Ward M, et al. On the role of melt flow into the surface structure and porosity development during selective laser melting. *Acta Mater.* 2015;96:72–79. DOI: [10.1016/j.actamat.2015.06.004](https://doi.org/10.1016/j.actamat.2015.06.004)
  - [14] Pei W, Zhengying W, Zhen C, et al. Numerical simulation and parametric analysis of selective laser melting process of AlSi10Mg powder. *Appl Phys A.* 2017;123. DOI: [10.1007/s00339-017-1143-7](https://doi.org/10.1007/s00339-017-1143-7)
  - [15] Wei HL, Mukherjee T, Zhang W, et al. Mechanistic models for additive manufacturing of metallic components. *Prog Mater Sci.* 2020; 100703. DOI: [10.1016/j.pmatsci.2020.100703](https://doi.org/10.1016/j.pmatsci.2020.100703)
  - [16] Mukherjee T, DebRoy T. Mitigation of lack of fusion defects in powder bed fusion additive manufacturing. *J Manuf Process.* 2018;36:442–449. DOI: [10.1016/j.jmapro.2018.10.028](https://doi.org/10.1016/j.jmapro.2018.10.028)
  - [17] Promopatum P, Yao S-C. Analytical evaluation of defect generation for selective laser melting of metals. *Int J Adv Manuf Technol.* 2019;103(1–4):1185–1198. DOI: [10.1007/s00170-019-03500-z](https://doi.org/10.1007/s00170-019-03500-z)
  - [18] Wang W, Ning J, Liang SY. Prediction of lack-of-fusion porosity in laser powder-bed fusion considering boundary conditions and sensitivity to laser power absorption. *Int J Adv Manuf Technol.* 2021;112(1–2):61–70. DOI: [10.1007/s00170-020-06224-7](https://doi.org/10.1007/s00170-020-06224-7)
  - [19] Zagade P, Gautham BP, De A, et al. Analytical estimation of fusion zone dimensions and cooling rates in part scale laser powder bed fusion. *Addit Manuf.* 2021;46:102222. DOI: [10.1016/j.addma.2021.102222](https://doi.org/10.1016/j.addma.2021.102222)
  - [20] Gong H, Rafi K, Gu H, et al. Analysis of defect generation in Ti-6Al-4 V parts made using powder bed fusion additive manufacturing processes. *Addit Manuf.* 2014;1–4:87–98. DOI: [10.1016/j.addma.2014.08.002](https://doi.org/10.1016/j.addma.2014.08.002)
  - [21] Choi J-P, Shin G-H, Yang S, et al. Densification and microstructural investigation of Inconel 718 parts fabricated by selective laser melting. *Powder Technol.* 2017;310:60–66. DOI: [10.1016/j.powtec.2017.01.030](https://doi.org/10.1016/j.powtec.2017.01.030)
  - [22] Simmons JC, Chen X, Azizi A, et al. Influence of processing and microstructure on the local and bulk thermal conductivity of selective laser melted 316L stainless steel. *Addit Manuf.* 2020;32:100996. DOI: [10.1016/j.addma.2019.100996](https://doi.org/10.1016/j.addma.2019.100996)
  - [23] Vallejo N D, Lucas C, Ayers N, et al. Process optimization and microstructure analysis to understand laser powder bed fusion of 316L stainless steel. *Metals.* 2021;11(5):832. DOI: [10.3390/met11050832](https://doi.org/10.3390/met11050832)
  - [24] Dilip JJS, Zhang S, Teng C, et al. Influence of processing parameters on the evolution of melt pool, porosity, and microstructures in Ti-6Al-4 V alloy parts fabricated by selective laser melting. *Prog Addit Manuf.* 2017;2(3):157–167. DOI: [10.1007/s40964-017-0030-2](https://doi.org/10.1007/s40964-017-0030-2)
  - [25] Choi J-P, Shin G-H, Brochu M, et al. Densification behavior of 316L stainless steel parts fabricated by selective laser melting by variation in laser energy density. *Mater Trans.* 2016;57(11):1952–1959. DOI: [10.2320/matertrans.M2016284](https://doi.org/10.2320/matertrans.M2016284)
  - [26] Yakout M, Elbestawi MA, Veldhuis SC. Density and mechanical properties in selective laser melting of invar 36 and stainless steel 316L. *J Mater Process Technol.* 2019;266:397–420. DOI: [10.1016/j.jmatprotec.2018.11.006](https://doi.org/10.1016/j.jmatprotec.2018.11.006)
  - [27] Hyer H, Zhou L, Park S, et al. Understanding the laser powder bed fusion of AlSi10Mg alloy. *Metallogr Microstruct Anal.* 2020;9(4):484–502. DOI: [10.1007/s13632-020-00659-w](https://doi.org/10.1007/s13632-020-00659-w)
  - [28] Narvan M, Al-Rubaie KS, Elbestawi M. Process-structure-property relationships of AISI H13 tool steel processed with selective laser melting. *Materials.* 2019;12(14):2284. DOI: [10.3390/ma12142284](https://doi.org/10.3390/ma12142284)
  - [29] Narvan M, Ghasemi A, Fereiduni E, et al. Part deflection and residual stresses in laser powder bed fusion of H13 tool steel. *Mater Des.* 2021;204:109659. DOI: [10.1016/j.matdes.2021.109659](https://doi.org/10.1016/j.matdes.2021.109659)
  - [30] Balbaa M, Mekhiel S, Elbestawi M, et al. On selective laser melting of Inconel 718: densification, surface roughness, and residual stresses. *Mater Des.* 2020;193:108818. DOI: [10.1016/j.matdes.2020.108818](https://doi.org/10.1016/j.matdes.2020.108818)
  - [31] Rai R, Elmer JW, Palmer TA, et al. Heat transfer and fluid flow during keyhole mode laser welding of tantalum, Ti-6Al-4 V, 304L stainless steel and vanadium. *J Phys Appl Phys.* 2007;40(18):5753–5766. DOI: [10.1088/0022-3727/40/18/037](https://doi.org/10.1088/0022-3727/40/18/037)
  - [32] Mills KC. Recommended values of thermophysical properties for selected commercial alloys. Cambridge: Woodhead Publishing; 2002.



- [33] Kabir IR, Yin D, Tamanna N, et al. Thermomechanical modelling of laser surface glazing for H13 tool steel. *Appl Phys A*. 2018;124(3):260. DOI: 10.1007/s00339-018-1671-9
- [34] Freedman DR, Pisani R, Purves R. *Statistics*. 4th ed New York: W. W. Norton & Company; 2007.
- [35] Taylor R. Interpretation of the correlation coefficient: a basic review. *J Diagn Med Sonogr*. 1990;6(1):35–39.
- [36] Jamnikar ND, Liu S, Brice C, et al. In situ microstructure property prediction by modeling molten pool-quality relations for wire-feed laser additive manufacturing. *J Manuf Process*. 2022;79:803–814. DOI: 10.1016/j.jma.2022.05.013
- [37] Wen C, Zhang Y, Wang C, et al. Machine learning assisted design of high entropy alloys with desired property. *Acta Mater*. 2019;170:109–117. DOI: 10.1016/j.actamat.2019.03.010
- [38] Dai D, Xu T, Wei X, et al. Using machine learning and feature engineering to characterize limited material datasets of high-entropy alloys. *Comput Mater Sci*. 2020;175:109618. DOI: 10.1016/j.commatsci.2020.10.9618
- [39] Guzmán J, Nobre R, Nunes ER, et al. Laser powder bed fusion parameters to produce high-density Ti–53%Nb alloy using irregularly shaped powder from hydride-dehydride (HDH) process. *J Mater Res Technol*. 2021;10:1372–1381. DOI: 10.1016/j.jmrt.2020.12.084
- [40] Eschner N, Weiser L, Häfner B, et al. Classification of specimen density in laser powder bed fusion (L-PBF) using in-process structure-borne acoustic process emissions. *Addit Manuf*. 2020;34:101324. DOI: 10.1016/j.addma.2020.101324
- [41] Kumar P, Farah J, Akram J, et al. Influence of laser processing parameters on porosity in Inconel 718 during additive manufacturing. *Int J Adv Manuf Technol*. 2019;103(1–4):1497–1507. DOI: 10.1007/s00170-019-03655-9
- [42] Véle F, Ackermann M, Bittner V, et al. Influence of selective laser melting technology process parameters on porosity and hardness of AISI H13 tool steel: statistical approach. *Materials (Basel)*. 2021;14(20):6052. DOI: 10.3390/ma14206052

## Appendix. Formulation of dimensionless variables

The dimensional analysis involves eight variables and three fundamental dimensions (M, L, and T) as shown in Table 1. Five (8 - 3) dimensionless terms are therefore formed following Buckingham's  $\pi$ -theorem. The variable porosity fraction

( $\phi$ ) is dimensionless and considered as

$$\pi_1 = \phi \quad (A1)$$

Using three repeatable variables as  $P$ ,  $v$ , and  $\lambda$ , the next two dimensionless terms are written as

$$\pi_{21} = P^a v^b \lambda^c \delta^i \quad (A2)$$

$$\pi_{22} = P^a v^b \lambda^c w^j \quad (A3)$$

The exponents in Equations (A2–A3) are solved by writing these equations in a dimensional form that results in  $\pi_{21} = \lambda/\delta$  and  $\pi_{22} = \lambda/w$ . A ratio of  $\pi_{22}$  and  $\pi_{21}$  results in a dimensionless term  $\delta/w$ , which depicts a ratio of the hatch spacing and the melt pool width, and bears a measure of lack-of-fusion porosity as reported in the literature [9,16]. Thus, the second dimensionless term is considered as

$$\pi_2 = \frac{\delta}{w} \quad (A4)$$

Likewise, the next dimensionless variable is written considering the same repeatable variables as

$$\pi_3 = P^a v^b \lambda^c d^k \quad (A5)$$

which on further simplification results in

$$\pi_3 = \frac{\lambda}{d} \quad (A6)$$

Equation (A6) shows that  $\pi_3$  presents a ratio of the layer thickness and the melt pool depth, which is also reported to be an important variable to assess lack-of-fusion porosity in the literature [9,16]. The last dimensionless variable is written as

$$\pi_4 = P^a v^b \lambda^c H_m^l \quad (A7)$$

that can be written after further simplification as

$$\pi_4 = \frac{P}{(v\lambda^2)H_m} \quad (A8)$$

Considering further that the hatch spacing  $\delta$  and the layer thickness  $\lambda$  have the same dimension, the variable group  $(v\lambda^2)$  in the denominator of Equation (A8) is rearranged as  $(v\delta\lambda)$  to include all the three characteristic dimensions in the scanning, hatching and building directions through the variables  $v$ ,  $\delta$ , and  $\lambda$ , respectively. The resulting term  $P/(v\delta\lambda)$  is oftentimes referred to as the input energy density in literature [20,24] and accordingly, the fourth dimensionless term is rewritten as

$$\pi_4 = \frac{P}{(v\delta\lambda)} \frac{1}{H_m} \quad (A9)$$